IRAQI BULLETIN OF GEOLOGY AND MINING (IBGM)\
IRAQ GEOLOGICAL SURVEY (GEOSURV-IRAQ)

*IBGM (**2025**, Vol 21; Issue 2)* *179-201*

GEOCHEMICAL CHARACTERISTICS AND GENESIS OF COPPER MINERALIZATION IN MAFIC ROCKS OF THE GALALLA AREA, SORAN DISTRICT, KURDISTAN REGION, IRAQ

Mohammad Piroui

Department of Petroleum Geosciences, Faculty of Science, Soran University, Kurdistan Region, Iraq
Correspondence: mohammad.askandar@soran.edu.iq; Mohammad Piroui

Type of the Paper (Article)
Received: 02/05/2025
Accepted: 01/06/2025
Available online: 27/12/2025

Abstract

This investigation reveals new copper mineralization in the Galalla area of the Kurdistan Region. The mineralization is hosted by basaltic and gabbroic rock and is situated within the structural framework of the Iraqi Zagros Suture Zone. In this study, the integration of field geology, petrography, XRD, SEM-EDS, and whole-rock geochemistry was applied to investigate the nature and evolution of mineralization. The assemblages of minerals, such as chlorite, albite, epidote, and quartz, show widespread hydrothermal alteration. The ore minerals include chalcopyrite, chalcocite, covellite, malachite, chrysocolla, and Cu-bearing hematite and magnetite. These minerals display textures such as replacement, which are spatially associated with alteration minerals, indicating metal mobilization by hydrothermal fluids. Copper concentration in the rocks ranges from 33 to 7536 ppm, with the elevation of other elements such as Fe_2O_3, and enrichment of LREE (e.g., La, Ce, and Nd). The presence of Cu in the P-rich minerals may be related to hydrothermal alteration. The negative Eu anomalies suggest fluid-driven remobilization. Based on this evidence, mineralization in Galalla resulted from a multi-stage evolution involving magmatic precursors followed by hydrothermal alteration and supergene enrichment. The findings will upgrade the potential economic importance of the Galalla area and warrant further exploration techniques.

Keywords: Galalla; Copper Mineralization; Hydrothermal Alteration; Sulfides.

1. Introduction

The sediment-hosted copper deposits, porphyry copper deposits, volcanogenic massive sulfide deposits, and magmatic sulfide deposits are different types of copper mineralization (Cox et al., 2003; Sillitoe, 2010). These deposits can form by different geological processes, such as hydrothermal fluid, magmatic differentiation, and sedimentary diagenesis. Around 60 – 70% of copper production in the world comes from the sulfides that formed during the late magmatic and hydrothermal stages (Cannell, 2005).

ISSN 1811-4539, EISSN 3005-3714
https://doi.org/10.59150/ibgm2102a10
IBGM: http://ibgm-iq.org/
Academic Scientific Journals: www.iasj.net

Different types of ore mineralization, such as magmatic, hydrothermal, sedimentary, and metamorphic deposits, have been formed in the Kurdistan region. These mineralizations are of different types, including chromium, iron, copper, and manganese (Ismail, 2008; Mohammad & Yara, 2018; Ahmed et al., 2020; Pirouei et al., 2021; Latif et al., 2022; Mustafa et al., 2023a; Merza & Abdalla, 2023; Mohammad et al., 2024). The copper mineralization in the region is complex and is linked to its geological and tectonic history. The region's tectonic activity led to the formation of hydrothermal systems, which are important for the mineralization of copper and other metals. These systems of mineralization are usually accompanied by fault and shear zones that provide pathways for fluids that are rich in metals (Yassin et al., 2015). The Cu ore minerals are usually chalcopyrite, covellite, malachite, azurite, and bornite. The style of minerals of this nature is frequently hydrothermal veins or disseminated within the surrounding host rocks (Yassin et al., 2015; Mirza & Rashid, 2018; Mohammad & Yara, 2018; Pirouei et al., 2021; Mustafa et al., 2023).

Mineralization of Fe, Cu, and Ni has been reported by previous investigations. Recently, Mustafa et al. (2023a, 2023b) reported new mineralizations of oxide and sulfide minerals in the northern and northwestern parts of Galalla. According to their study, mineralization exhibits a strong connection with Paleogene magmatic and hydrothermal processes, which are notably affected by the structural dynamics of fractures and faults within the geological framework. This study reveals that the existence of secondary copper minerals, including malachite and azurite, is a sign of supergene enrichment processes besides the initial primary sulfide mineralization.

The present study will focus on another newly discovered copper mineralization in the western part of the Galalla area. The mineralization occurs in gabbro and basalt. This research will apply field observations, petrography, and geochemical analyses to explore the characteristics of the newly discovered mineralization and compare it with previously explored mineralizations in the Galalla.

2. Geological Setting

2.2. Regional Geological and Tectonic

The study area is situated in northeastern Iraq, in the vicinity of Galalla village (Figure 1). Tectonically, this region falls within the Iraqi Zagros Suture Zone (IZSZ), which represents one of the intensely deformed areas due to the ongoing convergence between the Arabian and Anatolian microplates to the north, as well as the Arabian and Iranian continental plates in the NE of Iraq (Numan, 1997). On a broader scale, the IZSZ is a component of the Alpine-Himalayan orogenic belt (See Figure 1a) (Alavi, 1994, 2004; Othman and Gloaguen, 2013).(Alavi, 1994, 2004; Othman & Gloaguen, 2013; Mohammad et al., 2014; Mohammad & Cornell, 2017). The tectonic units of the suture zone are Shalair, Penjwen-Walash, and Qulqula-Khwakurk (Jassim & Guff, 2006; Lawa et al., 2013) (refer to Figure 1b).

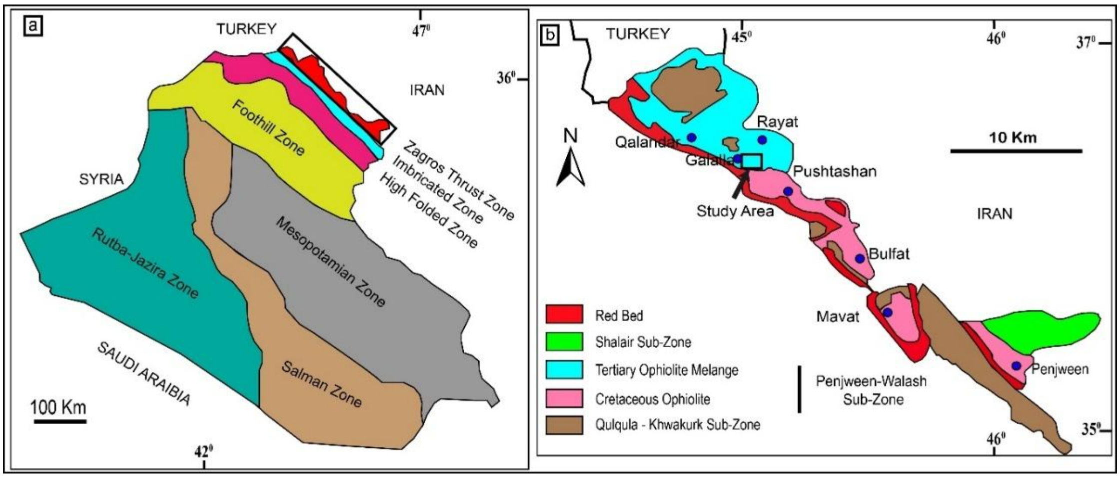

Figure 1. a) Simplified geological map of the Iraqi Zagros Suture Zone along the Iraq-Iran border (after Moores et al., 2000 and modified by Sissakian, 2000), b) detailed geological map of the broader Rayat area, NE Iraq (modified by Sissakian, 2000).

The area is a part of the Penjween-Walash Subzone, located within the Walash Group. The Walash Group is generally composed of sedimentary rocks (such as argillites, ferruginous conglomerates, and red siliceous-jasper rocks), volcano-sedimentary rocks, and igneous rocks (Vasieliev M.M. Pentelikov, 1962). The igneous rocks consist of serpentinized peridotites, along with listvenites and fuchsite, formed through hydrothermal alteration (Pirouei et al., 2020). The volcanic rocks range from basalts to andesites (Al-Qayim et al., 2014; Mohammad et al., 2023; Mustafa et al., 2023).

The age of the Walash Group, based on the ^{40}Ar-^{39}Ar on basaltic rocks, is in the range of 24 – 43Ma (Ali et al., 2012). Further studies of volcanic rocks from the Mawat nappes suggest two magmatic phases: an andesitic phase 43.01 ± 0.15 Ma, followed by an extensional arc phase around 32.31 ± 0.60 Ma (Aswad et al., 2014). Recently, Mohammad et al. (2023) proposed the age of Cretaceous to Paleocene (69.7 ± 2.7 Ma) for the Walash Group by using zircon U-Pb dating.

2.2. Local geology and field descriptions

In the Walash Group, the volcanic rocks are categorized into several groups: basic dykes, lava flows, and pillow lavas, which predominantly consist of spilitic diabase along with pyroxene-bearing spilitic basalt and spilite, as well as intermediate volcanic rocks that include varieties such as andesite, andesite, and intercalated pyroclastic rocks with sediments (Jassim & Guff, 2006). Geologically, the Galalla area is composed of volcanic rocks, principally basalt and andesite, which are associated with red sedimentary layers. These volcanic units exhibit color variations from grayish to green and brownish-gray. They are notable for their substantial, fractured to brecciated textures and are cross-cut by quartz and calcite veins, further highlighting their complex structural history (Mustafa et al., 2023a, 2023b).

The volcanic rocks are covered by layers of conglomerates and pyroclastic deposits. In addition, red siliceous carbonates occur as discrete patches or lens-shaped bodies that interlace with the underlying igneous rocks. Moreover, red radiolarian cherts (with a thickness of approximately 2 meters and stretching more than 1 kilometer in length) are found in association with the volcanic series (Mustafa et al., 2023a). Al-Jubury et al. (2023) describe the ultramafic rocks of the area as comprising dunite and harzburgite, and their geochemical analyses indicate that these rocks bear characteristics typical of ophiolitic ultramafic formations.

The studied section, in this study, is composed of different rocks, including ultramafic rocks, such as serpentinite, and mafic rocks, including basalt and gabbro (Figures 2 and 3a, b, and c). Mineralization occurred as chrysocolla and malachite in brecciated gabbro and basaltic rocks (Figures 3d and 3e). The basalts in the hand specimen show brecciation and mineralization of copper and iron mineralization is evident (Figure 4a and b). The gabbro is highly altered (Figure 4c and d) and in some parts is brecciated. As it is clear in Figure 4, both gabbro and basalt experienced a high degree of alteration, including epidotization, chloritization, hematitization, silicification, and carbonatization. Probably most of the basalts are converted to the spilite.

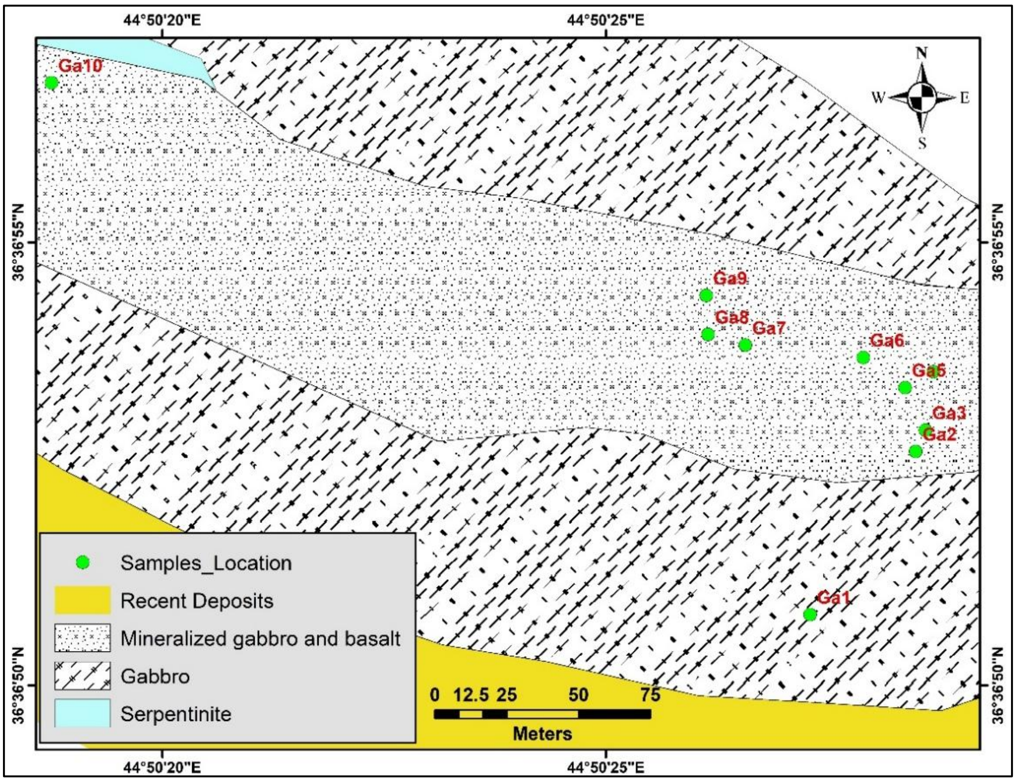

Figure 2. Detailed geological map of the section in Galalla according to this study.

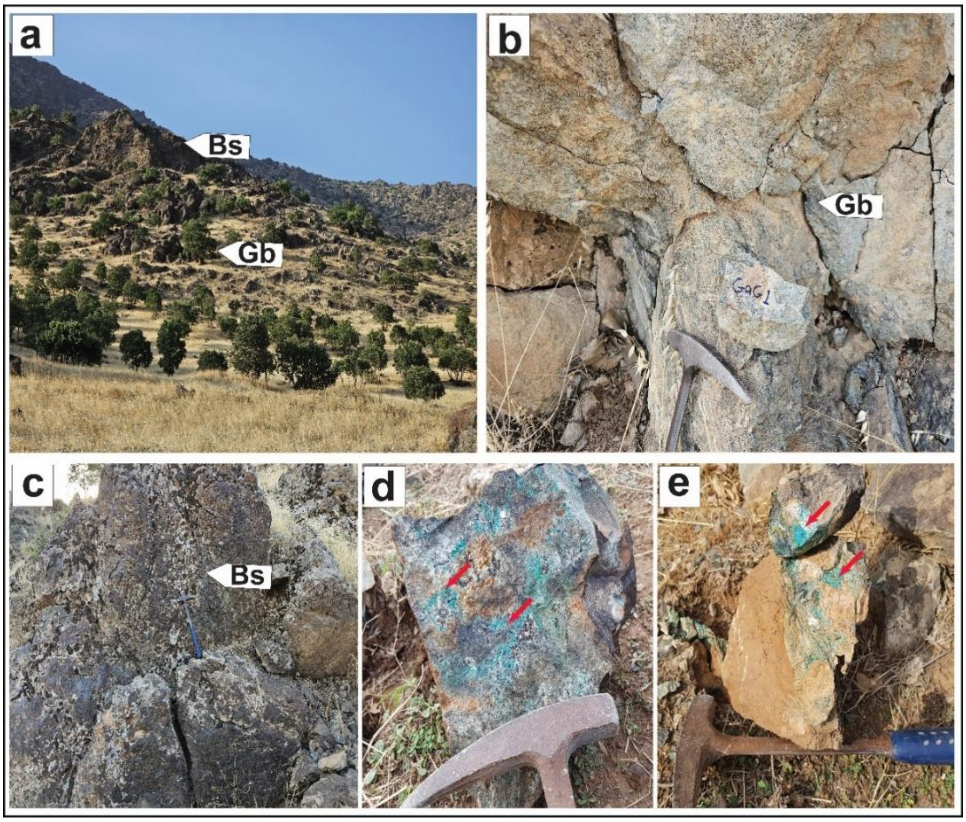

Figure 3. (a) An overview of the gabbro and basalt in the study area (The view is oriented northeast); (b and c) outcrop photographs of gabbro and basalt, respectively; and (d and e) represent the mineralization of chrysocolla and malachite, respectively, in the rocks of the area.

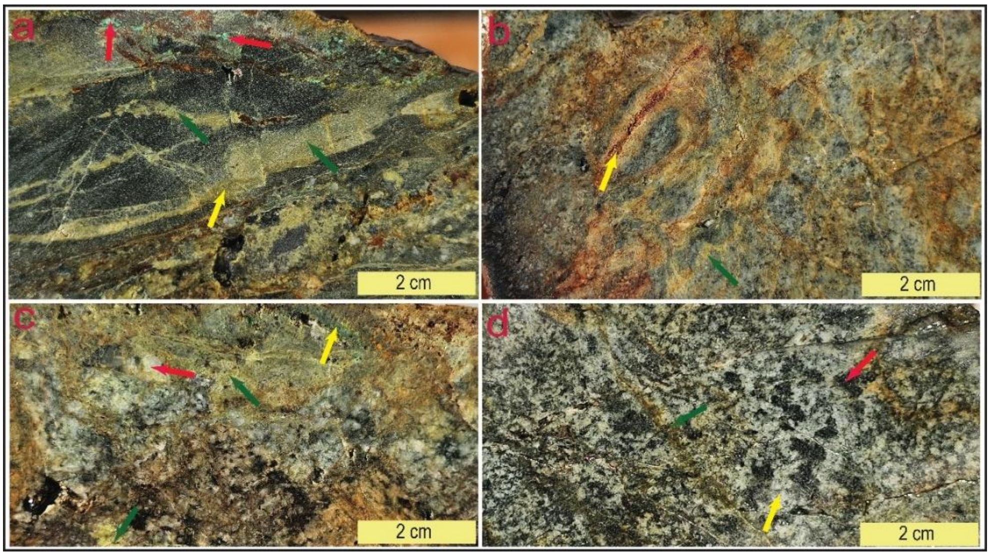

Figure 4. Macrophotographs of the different rock samples of the area. (a and b) altered basalts (spilite) of the area. In the figure, a mineralization of chrysocolla (red arrows) is evident; the other minerals are epidote (Green arrows) and Chlorite. Figure b shows iron oxide mineralization (Yellow arrow) and alteration minerals such as epidote (green arrow); (c) is an altered gabbro with chrysocolla mineralization (Yellow arrow), Calcite (red arrow), and epidote (green arrows); and (d) showing an altered gabbro contain plagioclase (Yellow arrow) and pyroxene (red arrow), epidote and chlorite (green arrow).

3. Materials and methods

This study involved a comprehensive field investigation within the study area, during which 10 samples of mineralized gabbro and basalt were collected. Concurrently, a detailed geological map covering the study area was prepared (Figure 2). Each sample was cut, and thin-polished sections were made from it and then examined using an optical microscope to study their petrographic features, with a particular emphasis on distinguishing mineral assemblages and textural characteristics. In addition, X-ray diffraction (XRD) analyses were conducted on all collected samples at Soran University, utilizing a PANalytical X'Pert PRO MPD Alpha1 powder diffractometer. The resulting diffraction data were subsequently evaluated qualitatively and semi-quantitatively using High-Score Plus software. To supplement the identification of individual minerals and their chemical compositions, scanning electron microscopy (FEI 480) supplied with energy dispersive X-ray spectroscopy (SEM-EDS) was employed. Furthermore, geochemical analyses were done on powdered samples at Zarazma Laboratory in Iran. Inductively Coupled Plasma Optical Emission Spectroscopy (ICP-OES) was used for major elements, and Inductively Coupled Plasma Mass Spectrometry (ICP-MS) for trace and rare earth elements. Before analysis, nearly complete sample digestion was achieved through a four-acid (including hydrofluoric, hydrochloric acid, perchloric acid, and nitric acid).

4. Results

4.1. Mineralogy, petrography, and mineral chemistry

The rocks in the study area are highly altered, and to identify all mineral components of the rock in a good way, three techniques, including optical microscopy, XRD, and SEM-EDS, were used. The petrographic analysis provides insights into mineralogy and textures, highlighting primary and secondary mineral assemblages of the study area mineralizations and rocks.

4.1.1. Mineralogy and Petrography of Basalt

The Galalla basalts (Ga4, Ga6-Ga10) exhibit different mineralogy and textures due to hydrothermal alteration and low-grade metamorphism, as confirmed by XRD and optical microscopy. The major minerals of the basalt are epidote with the percentage of more than 35.2% (Figure 5a & and Table 1), and albite (9.7 – 60.5%) (Figure 5d). The other major components are quartz (2% – 42.4%) and chlorite, with an amount of 1.8 – 28.2% in XRD calculation (Table 1). The actinolite and tremolite are only present in sample Ga4, showing the amounts of 41.5% and 12%, respectively. The minor minerals are calcite (Figure 5b), zoisite (Figure 5c), and clinopyroxene (Table 1).

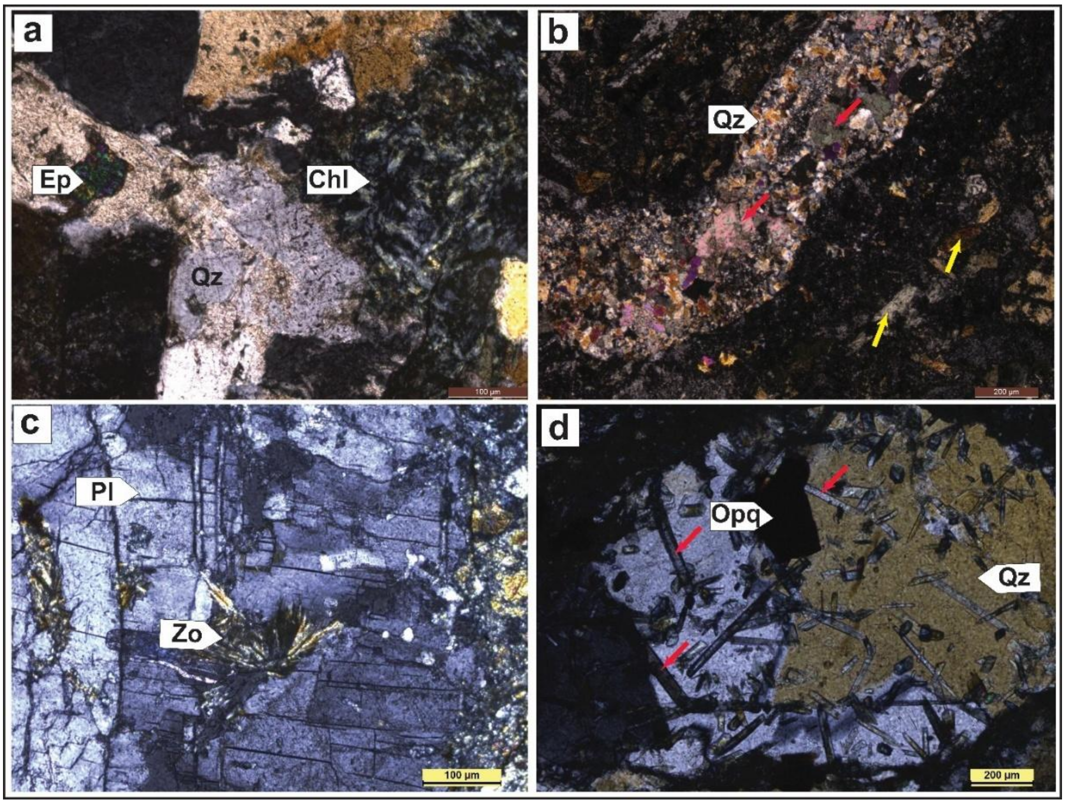

Figure 5. Microphotograph of basalt in the Galalla area. (a) Chloritization and Epidotization of the feldspars; (b) presence of associated quartz and calcite (red arrows) veins and actinolite (yellow arrows) in the altered basalt; (c) saussuritization of plagioclases to zoisite; and (d) albitization and silicification of basalts. (Abbreviations: Ep (epidote); Chl (Chlorite); Qz (quartz); Pl (plagioclase); Zo (zoisite); and Opq (Opaque mineral).

Table 1. XRD results of different rocks in the studied area (Gb: Gabbro and Bs: Basalt).

Sample	**Ga1**	**Ga2**	**Ga3**	**Ga4**	**Ga5**	**Ga6**	**Ga7**	**Ga8**	**Ga9**	**Ga10**
Rock	**Gb**	**Gb**	**Gb**	**Bs**	**Gb**	**Bs**	**Bs**	**Bs**	**Bs**	**Bs**
Actinolite	-	-	-	41.5	-	-	-	-	-	-
Albite	21.2	46.2		34.1	35.8	25.3	60.5	31.6	9.7	42.6
Anorthite	18.7	-	-	-	-	-	-	-	-	-
Clinopyroxene	30.7	-	52.8	-	-	0.5	-	-	-	-
Calcite	-	-	-	0.3	-	-	-	-	-	0.2
Chlorite	26.9	2.2	2.5	7.1	-	1.8	14	28.2	27.8	3
Enstatite	-	0.3	4	-	-	-	-	-	-	-
Epidote	2.5	14.2	3.2	3.1	22.6	35.2	23.7	26	31.9	-
Quartz	-	37	37.5	2	41.3	37.3	-	12.5	30.6	42.4
Tremolite	-	-	-	12	-	-	-	-	-	-
Zoisite	-	-	-	-	-	-	1.8	1.6	-	11.9

Petrographically, the basalts display fine-grained intergranular to hypidiomorphic granular textures, where primary plagioclase (now mostly albite) forms a crystalline framework, while clinopyroxenes are either absent or extensively replaced. Chlorite and actinolite replace primary clinopyroxenes. The fine-grained nature of these basalts supports a rapid cooling origin, but subsequent saussuritization of plagioclase (Figure 5c) and silicification (Figure 5b & d) suggest hydrothermal overprinting.

4.1.2. Mineralogy and petrography of gabbro

The Galalla gabbro (Ga1-Ga3 and G5) exhibits a coarse-grained subophitic and granular texture, confirming slow cooling from a plutonic mafic magma. The major minerals identified include albite (21.2 – 46.2%), clinopyroxene (30.7 – 52.8%) (Figure 6a & d), epidote (2.5 – 14.2%) (Figure 6b), and quartz (up to 37.5%) (Figure 6b), with chlorite (2.2 – 26.9%). Plagioclase appears as subhedral to anhedral grains with signs of alteration, including saussuritization (replacement by epidote, Figure 6b). Clinopyroxenes exhibit fracturing and are partially replaced by chlorite (Figure 6a). Quartz occurs as veins (Figure 6b), and the other generation has been directly crystallized from magma with a triple junction (Figure 6c).

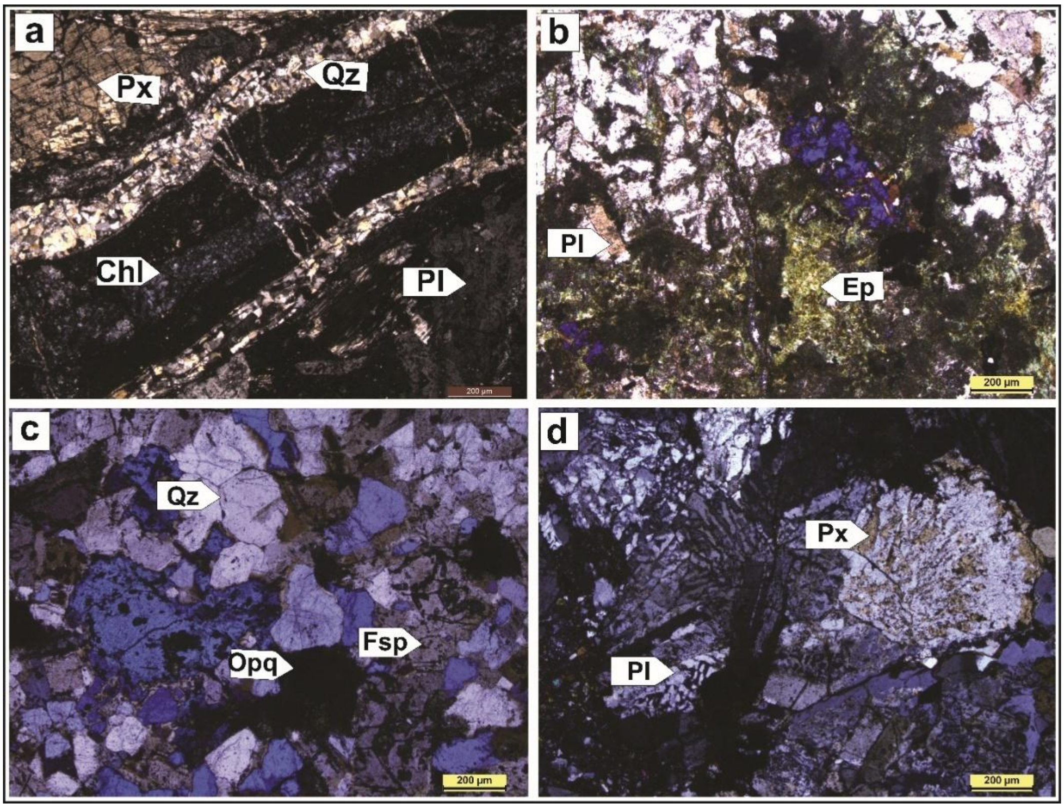

Figure 6. Mineral components of gabbro in the Galalla area. (a) large grain of pyroxene in the rock and partially altered to chlorite; (b) saussuritization of the plagioclase in the gabbro; (c) Presence of primary crystals of quartz in the gabbro, and scattered opaque minerals; and (d) intergrowth of plagioclase and pyroxene. (Abbreviations: Px (pyroxene); Qz (quartz); Chl (Chlorite); Pl (plagioclase); Ep (epidote); Fsp (feldspar); and Opq (Opaque mineral).

Opaque minerals (ranging from ~50 – 200 µm in size) are scattered within the matrix and appear to be sulfides and Fe-oxides (Figure 6c). The alteration processes are dominated by chloritization (Figure 6a), saussuritization of plagioclase (Figure 6b), and silica enrichment (interstitial quartz, Figure 6a & c). The intergrowth of plagioclase and clinopyroxene (Figure 6d) suggests equilibrium crystallization, confirming the gabbroic nature of the rock.

4.1.3. Ore Mineralogy and Mineral Chemistry

The ore minerals exhibit complex mineralization in terms of textures, replacement, and alteration features. Hematite, chalcopyrite, and magnetite are the dominant opaque minerals (Figure 7a-e). Hematite is formed as colloform and botryoidal textures (Figure 8a). Chalcopyrite (Figure 7c-d) appears as irregular patches with replacement textures, commonly rimmed or altered to covellite, hematite, and magnetite (Figure 8). Chrysocolla is mostly formed as vein and fracture filling in both basalt and gabbro (Figure 7f).

SEM-EDS analysis further confirms chalcocite, covellite, and Cu-enriched hematite and magnetite, with Fe-Cu-S phases displaying zonal alteration patterns. Elemental mapping (Figure 8) reveals a strong Cu distribution in chalcocite, covellite, and malachite, while Fe dominates hematite and magnetite phases. The SEM-EDS analysis (Table 2) confirms chalcocite with Cu 83.1 % on average and S 12.4 % on average, while chalcopyrite contains 34.4 % on average. Cu and 31.8 % on average. S, with an average of 31.3% Fe. Cu-magnetite contains 29.3%, and Cu-hematite shows 13.7 % on average copper.

Table 2. SEM-EDS results of the ore minerals in the Galalla area.

Number of points	5	6	2	3	1	2	3	1	1
Mineral	**Chrysocolla**	**Cu - Magnetite**	**Cu-Hematite**	**Chalcopyrite**	**Chalcocite**	**Malachite**	**Pyrrhotite**	**Bornite**	**Covellite**
Mg	0.52	0.16	0.00	0.00	0.20	0.00	0.04	0.01	0.00
Al	5.62	1.33	0.59	0.36	0.37	0.19	0.04	1.81	0.11
Si	30.46	10.80	4.83	0.47	0.60	0.38	0.53	3.76	0.30
S	0.35	0.35	0.46	31.79	12.41	1.88	39.96	17.95	26.62
K	0.29	0.07	0.17	0.07	0.09	0.16	0.06	0.10	0.16
Ca	1.31	0.62	0.62	0.22	0.04	0.02	0.29	0.60	0.11
Ti	0.03	0.01	0.04	0.03	0.00	0.00	0.01	0.07	0.00
V	0.03	0.05	0.02	0.02	0.18	0.00	0.08	0.00	0.00
Mn	0.03	0.01	0.07	0.03	0.00	0.00	0.05	0.05	0.02
Fe	1.50	55.20	76.71	31.29	2.36	0.15	54.28	40.78	4.63
Co	0.03	0.74	1.23	0.56	0.11	0.06	1.11	0.82	0.11
Ni	0.01	0.29	0.21	0.02	0.00	0.02	0.13	0.00	0.05
Cu	59.06	29.36	13.71	34.40	83.10	95.39	2.42	33.58	67.04
Zn	0.42	0.34	0.78	0.38	0.04	1.42	0.02	0.20	0.15
As	0.02	0.05	0.06	0.00	0.00	0.01	0.27	0.04	0.00
Sb	0.02	0.06	0.04	0.00	0.00	0.00	0.06	0.00	0.04
Pb	0.04	0.07	0.06	0.00	0.46	0.18	0.00	0.17	0.28

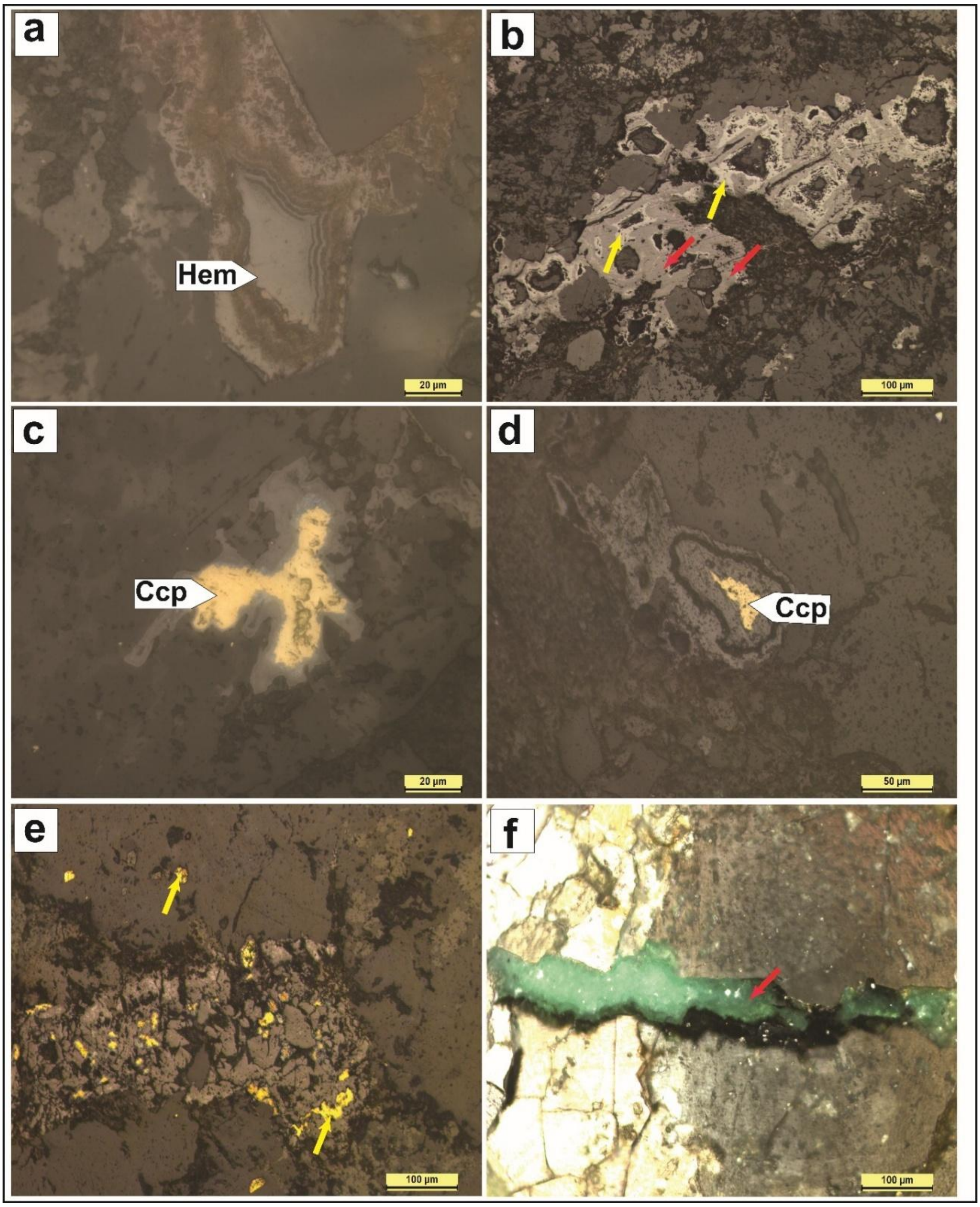

Figure 7. Microphotographs of the ore minerals in the gabbro and basalt of the Galalla area. a) Colloform texture of hematite; b) mineralization of magnetite (red arrows) and hematite (Yellow arrows) as vein and fracture filling; (c and d) decomposition of chalcopyrite to secondary minerals such as covellite (Figure c), hematite and magnetite (Figure d); e) disseminated chalcopyrite mineralization in host rock in fractures and as open space filling of the primary minerals; and (f) mineralization of chrysocolla as vein filling. [abbreviations: Hem (hematite) and Ccp (chalcopyrite)].

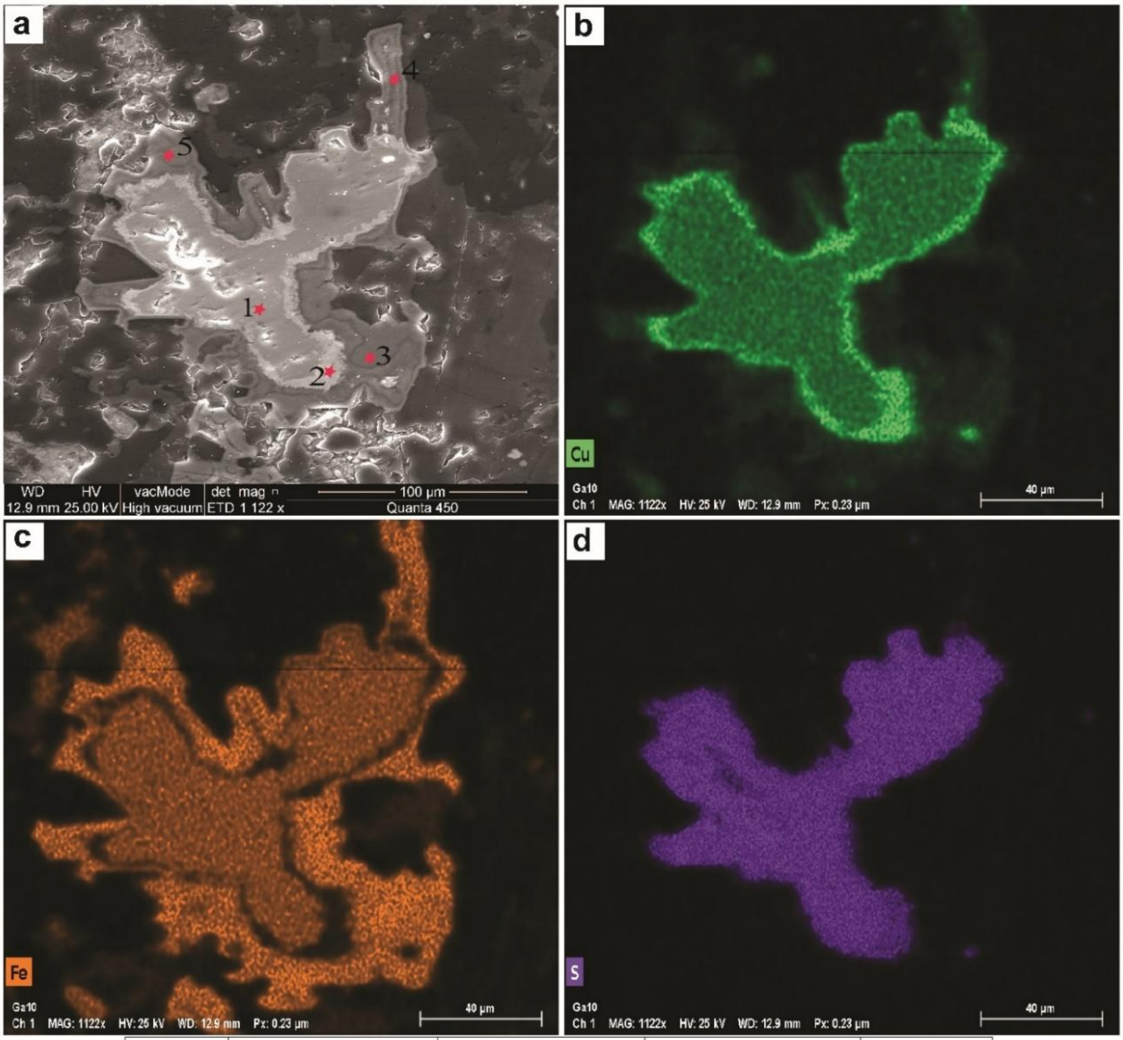

e	Cu	S	Fe	Mineral
1	33.02	34.92	29.72	Chalcopyrite
2	67.04	26.62	4.63	Covellite
3	13.94	0.53	76.47	Cu-Hematite
4	20.66	0.53	66.52	Cu-Magnetite
5	13.49	0.38	76.96	Cu-Hematite

Figure 8. SEM-EDS elemental mapping of the mineralized basalt. a) general view of the mapped slab with location of point analyzed; b) distribution map of copper, showing increasing concentration of Cu from core to the rims; c) distribution map of the Fe; d) distribution of S, and (e) results of point analyses of figure 9a with identified minerals.

The point analyses (Figure 9c) confirm the distinct chemistry of the identified minerals, with titanite being Ti-rich (37 – 47% TiO_2), hercynite characterized by high Fe_2O_3 (41.8%), and apatite containing significant P_2O_5 (40.7%) alongside CaO (57.02%). In contrast, the hydrothermal phosphate phase (Point 5) is enriched in P_2O_5 (59.75%) but significantly depleted in CaO (0.15%), suggesting a secondary formation process. Additionally, trace amounts of Cu (0.06%) in the hydrothermal phosphate indicate potential Cu enrichment associated with P remobilization in the system.

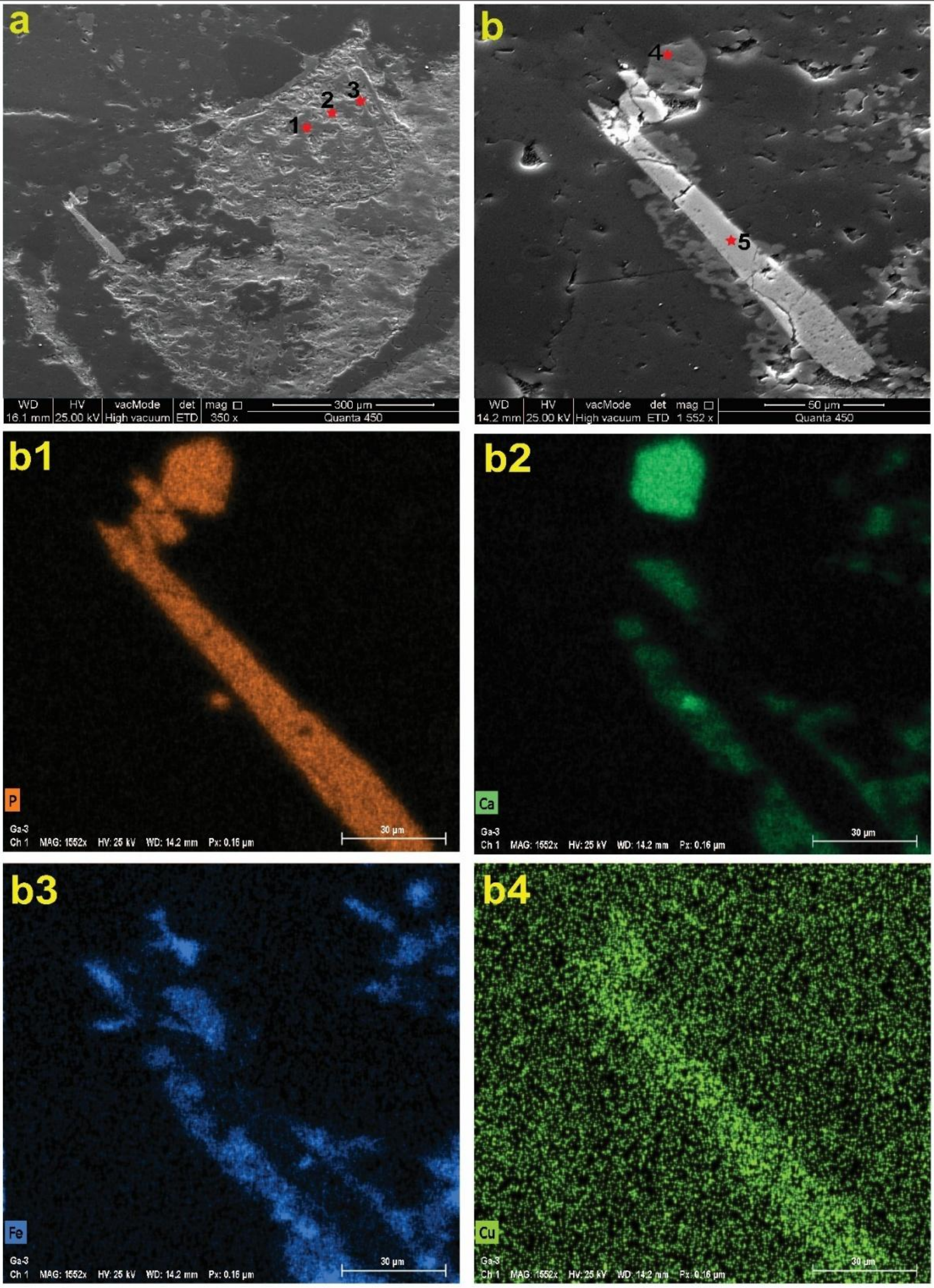

c

Points	Mineral	MgO	K_2O	CaO	TiO_2	Fe_2O_3	Al_2O_3	SiO_2	P_2O_5	Cu
1	Titanite	0.14	0.17	27.57	37.42	4.95	3.86	22.63		
2	Hercynite	5.02	0.38	0.83	0.96	41.83	25.38	22.49	0.07	
3	Titanite		0.00	26.01	47.71	4.79	1.03	18.19	0.25	
4	Apatite		0.32	57.02		0.35	0.05	0.76	40.67	0.04
5	Hydrothermal Phosphate		0.43	0.15		0.55	1.12	36.20	59.75	0.06

Figure 9. SEM-EDS elemental mapping of the mineralized gabbro. (a and b) general view of the mapped slabs with location of point analyzed; (b1-b4) distribution map of P, Ca, Fe, and Cu; and (c) results of point analyses of figure 10a and 10b with identified minerals.

4.2. Whole Rock Chemistry

The gabbro Samples (Ga1, Ga2, Ga3, Ga5) of the Galalla show SiO_2 in the range of 51.0% to 61.7%. Major elements such as CaO and MgO are present in the range of 2.7 – 11.8 and 0.77 – 10.6 %, respectively (Table 3). The Cu, Ni, Zn, and Co show concentration in the range of 125 to 2904 ppm, 2 to 151 ppm, 23 to 87 ppm, and 12.4 – 40.9 ppm, respectively. The REEs show moderate enrichment in LREE, while HREE are moderately depleted (Table 5).

Basalt (Ga4, Ga6, Ga7, Ga8, Ga9, Ga10) shows high SiO_2 concentrations ranging from 49.6% to 68.1%. The CaO and MgO contents are 3.63 – 8.1 and 0.94 – 8.02, respectively (Table 3). The Cu concentration range is 33 – 7536, while the concentration range for Zn, Ni, and Co is 58 – 315, 2 – 83, and 6.1 – 35.3, respectively (Table 4). Basalts are enriched in LREE (La, Ce, and Nd), but the concentration of HREE (Dy, Yb, and Lu) remains relatively low (Table 5).

The Galalla samples are highly altered, and they show an increase and depletion in some elements, such as SiO_2. For this reason, most diagrams for the discrimination of rock types cannot be used. Here, the diagram of Zr/TiO_2 vs. Nb/Y (Hastie et al., 2007) has been used (Figure 10) since the trace elements in the applied plot are highly immobile. According to the plot, all the samples are in the basalt (gabbro) range.

In all the samples of the Galalla, the (La/Yb) N > 1 means that LREE-enriched but HREE-depleted. The Ce anomaly in some samples is positive, and in some samples is negative, and Eu also shows the same condition, in some samples positive and some samples negative (Figure 11 and Table 5).

Table 3. ICP-OES results for major elements of samples for the Galalla area.

Element	Unit	DL	Ga1	Ga2	Ga3	Ga4	Ga5	Ga6	Ga7	Ga8	Ga9	Ga10
SiO_2	%	0.05	47.62	65.05	67.10	50.76	66.53	62.97	49.60	49.30	54.06	68.06
Al_2O_3	%	0.05	15.32	13.79	13.58	14.74	12.33	14.36	19.44	17.71	14.05	12.48
CaO	%	0.05	11.85	3.49	2.73	7.88	5.50	8.08	7.05	7.94	7.36	3.63
Fe_2O_3	%	0.05	6.94	8.08	6.91	10.10	8.13	8.31	11.87	13.30	13.60	7.33
K_2O	%	0.05	0.11	0.07	0.09	1.17	0.10	0.06	0.06	0.08	0.09	0.08
MgO	%	0.05	10.64	1.38	1.31	8.02	0.77	0.94	1.71	2.55	3.51	1.23
MnO	%	0.05	0.14	0.10	0.09	0.23	0.09	0.12	0.13	0.16	0.21	0.10
Na_2O	%	0.05	2.56	4.57	5.08	3.08	3.31	2.37	5.56	3.38	1.06	3.86
P_2O_5	%	0.05	0.05	0.18	0.14	0.09	0.06	0.05	0.20	0.28	0.15	0.08
TiO_2	%	0.05	0.30	0.64	0.54	1.02	0.43	0.34	0.82	0.95	1.07	0.42
LOI	%	0.05	4.46	2.51	2.09	2.90	2.33	2.16	3.04	3.55	3.85	2.26
Total			99.99	99.86	99.66	99.99	99.58	99.76	99.48	99.20	99.01	99.53

Table 4. ICP-OES results for trace elements of samples for the Galalla area.

Element	Unit	DL	Ga1	Ga2	Ga3	Ga4	Ga5	Ga6	Ga7	Ga8	Ga9	Ga10
Ag	ppm	0.1	0.1	0.1	0.4	0.1	0.2	0.5	0.4	0.6	0.4	0.1
As	ppm	0.5	3.5	3.1	6.8	2.5	6.9	6.1	16.7	12.7	19.8	8.1
Ba	ppm	1	32	56	61	174	30	30	25	31	28	38
Be	ppm	0.2	0.3	0.8	0.9	0.5	0.9	1.1	1	1	0.9	0.8
Cd	ppm	0.1	0.2	0.3	0.3	0.1	0.1	0.8	0.1	0.7	1	0.4
Co	ppm	1	40.9	13.1	17.4	34	12.4	6.1	18.3	22.3	35.3	13.5
Cr	ppm	1	683	49	40	288	39	32	16	78	50	36
Cs	ppm	0.5	0.5	0.5	0.5	0.6	0.5	0.5	0.5	0.5	0.5	0.5
Cu	ppm	1	125	952	1898	33	2904	1351	4609	4939	7536	3790
Hf	ppm	0.5	0.7	1.2	1.3	1.3	1.3	1.3	1.5	1.5	1.4	1.2
In	ppm	0.5	0.5	0.5	0.5	0.5	0.5	0.5	0.5	0.5	0.5	0.5
Li	ppm	1	12	9	9	10	8	11	10	12	12	10
Mo	ppm	0.5	0.5	0.6	0.5	0.5	0.5	0.8	1.1	1.8	0.8	0.9
Nb	ppm	1	3.2	6	4.8	3.8	6.5	7	11.7	9.3	5.7	6.5
Ni	ppm	1	151	5	2	83	3	3	1	3	14	2
Pb	ppm	1	2	1	1	3	1	2	4	4	4	2
Rb	ppm	1	2	1	1	21	1	1	1	1	1	1
S	ppm	50	181	251	474	155	501	229	208	532	675	453
Sb	ppm	0.5	0.5	0.5	0.5	0.5	0.6	0.5	0.6	0.6	0.6	0.5
Sn	ppm	0.1	1.5	1.5	1.3	1.5	1.5	3.1	3.8	3.3	1.8	1.6
Sr	ppm	1	111.5	114.4	112.3	190.7	245.8	320.1	272.5	238.6	211.2	108.5
Ta	ppm	0.1	0.3	0.4	0.2	0.3	0.4	0.5	0.7	0.6	0.4	0.4
Te	ppm	0.5	0.5	0.5	0.5	0.5	0.5	0.5	0.5	0.5	0.5	0.5
Th	ppm	0.1	1.2	1.3	1.4	1.2	1.4	1.3	1.7	1.4	1.2	1.5
Tl	ppm	0.1	0.1	0.1	0.1	0.1	0.1	0.1	0.1	0.1	0.1	0.1
U	ppm	0.1	0.1	0.2	0.2	0.1	0.2	0.1	0.3	0.2	0.4	0.2
V	ppm	1	154	11	8	212	12	19	8	16	163	9
Zn	ppm	1	40	23	48	60	87	158	64	126	315	58
Zr	ppm	5	10	29	44	32	33	31	37	40	33	29

Table 5. ICP-OES results for the rare earth elements of the samples for the Galalla area.

Element	Unit	DL	Ga1	Ga2	Ga3	Ga4	Ga5	Ga6	Ga7	Ga8	Ga9	Ga10
La	ppm	1	2	12	13	4	9	12	17	16	10	12
Ce	ppm	0.5	5	30	32	9	22	23	39	34	24	27
Pr	ppm	0.05	0.52	4.35	5.2	1.62	3.84	4.33	7.72	6.33	3.87	4.8
Nd	ppm	0.5	2.5	22.2	26.5	8.5	20.2	22.3	39.8	31.9	19.9	24.9
Sm	ppm	0.1	0.8	6.8	8	2.5	6.2	6.6	12.2	9.5	6	7.2
Eu	ppm	0.1	0.38	1.97	2.57	0.99	1.82	2.04	3.85	3.45	2.42	2.15
Gd	ppm	0.05	1.2	8.1	9.01	3.08	7.44	7.42	14.48	11.69	7.34	8.72
Sc	ppm	0.5	45.8	11.5	10.9	32.2	7.8	6.7	15	17	23.7	7.4
Tb	ppm	0.1	0.3	1.7	1.8	0.6	1.5	1.6	3	2.3	1.5	1.8
Dy	ppm	0.1	1.8	10.9	12	3.7	10.2	9.8	19.4	15.1	9.9	11.7
Er	ppm	0.1	1	6.5	7.2	2.4	6.2	5.7	11.9	9	6.1	7.2
Tm	ppm	0.1	0.2	0.9	1	0.4	0.9	0.9	1.6	1.2	0.9	1
Yb	ppm	0.05	0.96	6.14	6.53	2.08	6.44	5.71	11.33	8.27	5.87	7.06
Lu	ppm	0.1	0.2	0.8	0.9	0.4	0.9	0.9	1.5	1.2	0.8	1
Y	ppm	0.5	8.7	56.1	63.6	19.3	53.5	49.6	100.2	74.6	51.8	60.8
Ce/Ce*			1.19	1.01	0.95	0.86	0.91	0.77	0.83	0.82	0.94	0.86
Eu/Eu*			1.17	0.80	0.91	1.07	0.81	0.88	0.87	0.98	1.10	0.82
(La/Yb)N Ratio			1.66	1.56	1.59	1.54	1.12	1.68	1.20	1.55	1.36	1.36

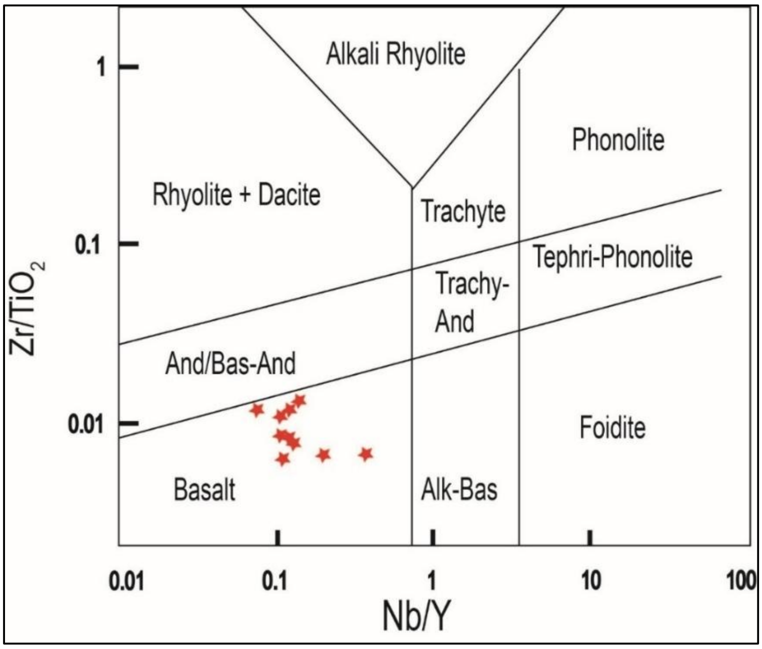

Figure 10. Basaltic and gabbroic rocks of the studied part in the Galalla area according to the Zr/TiO_2 vs. Nb/Y diagram (Hastie et al., 2007).

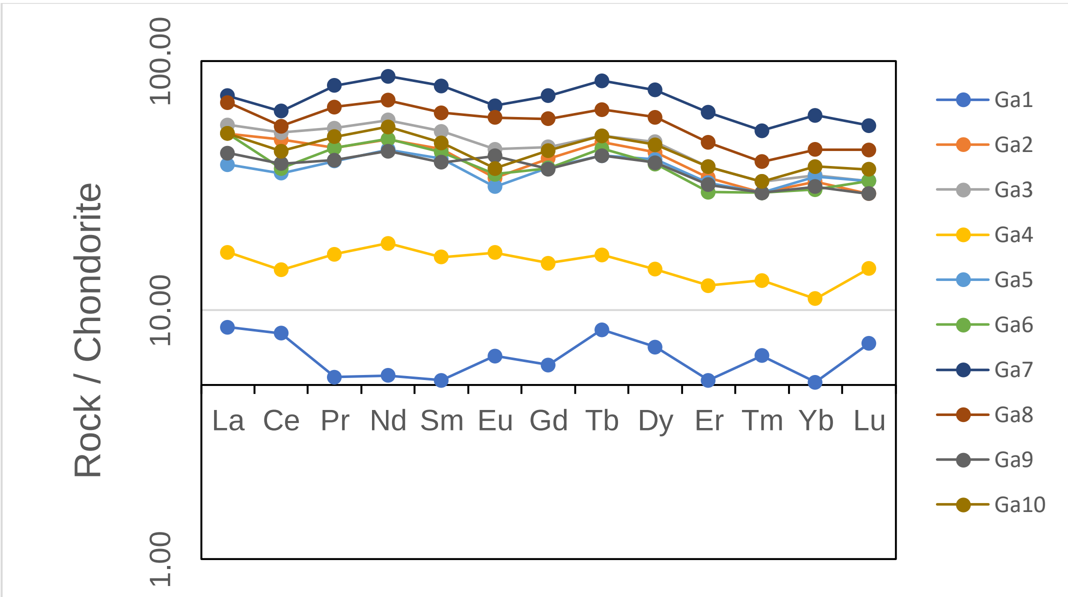

Figure 11. Chondrite-normalized REE patterns for Galalla samples according to (McDonough & Sun, 1995) values.

5. Discussion

5.1. Hydrothermal alteration, Mineralization type, Metal sources, and fluid Chemistry

5.1.1. Hydrothermal alteration

The deposition and transportation of metals can be greatly affected by hydrothermal alteration. Different mineralogical and geochemical transformations can occur by the interaction between hydrothermal fluids and surrounding rocks; these changes can be used as a key indicator for fluid pathways, metal sources, and ore formation processes (Sharkov et al., 2005; Simusokwe et al., 2021). Field observations show numerous alteration zones in mafic rocks. The alterations are silicification, chloritization, carbonation, and epidotization. Splitization is another alteration that happened in basaltic rocks; this alteration commonly occurs by hydrothermal fluid in the oceanic crust (Sharkov et al., 2005). Petrographic studies of the mineralized zones indicate a strong association between sulfide minerals (chalcopyrite, bornite, covellite) and alteration minerals (chlorite, epidote, calcite), indicating that mineralization formed during hydrothermal fluid circulation (Mondillo et al., 2020). The mineralization of titanite, magnetite, and apatite in mafic rocks suggests that the fluid mobilized and precipitated the metal, and this is compatible with findings on the influence of hydrothermal processes on iron sulfide minerals and the importance of these interactions in mineralization processes (Cao et al., 2019).

5.1.2. Metal sources, Fluid evolution, and Mineralization type

The data of trace element geochemistry, rare earth elements patterns, petrographic evidence, and the Eu anomalies can provide information about the metal source and fluid evolution. The presence of apatite, iron, and titanium oxides and titanite proposes that Cu, Fe, and P were at the beginning concentrated in the magmatic stage (Davidson et al., 2005). Apatite (with high CaO content) indicates that the P has been crystallized during the late stage of magmatic differentiation. The titanite, magnetite, and hercynite mineralization in gabbro recommend an early stage of metal enrichment, which can be considered as a primary source for metals in later hydrothermal mobilization (Pettke et al., 2010). The presence of alteration zones such as chloritization, epidotization, silicification, carbonation, and splitization supports the role of hydrothermal fluids in metal transport (Gao et al., 2024). The presence of tube-like hydrothermal phosphates, with high P_2O_5 (59.75%) and depleted CaO (0.15%), suggests P remobilization and reprecipitation from primary apatite (Todesco et al., 2010). The Cu distribution within phosphates (Figure 9) suggests that Cu was transported alongside P-bearing hydrothermal fluids, similar to processes observed in hydrothermal systems (Pitcairn et al., 2006). The formation of bornite and covellite (secondary Cu sulfides) and the presence of veins further support a hydrothermal source for Cu (Grosche et al., 2023). The light rare earth elements (LREE) enrichment and heavy rare earth elements (HREE) depletion pattern is a sign of fluid/rock interaction (Efimenko et al., 2014). The Eu with negative anomalies could be an indicator of hydrothermal fluids interaction with plagioclase, which led to the preferred mobilization of Eu^{2+} under reducing conditions (Bruno et al., 2007). The scattered Cu distribution in hydrothermally altered apatite suggests a fluid-related association between Cu and P, reflecting hydrothermal overprinting of earlier magmatic phases (Troll et al., 2019).

5.2. Paragenetic Sequence of Mineralization

Textural evidence and mineral relationships show a four-stage mineralization history including the magmatic Stage, Early Hydrothermal Stage, Late Hydrothermal Stage, and Supergene Stage (Figure 12). The presence of primary magnetite and accessory minerals such as titanite and apatite shows the early stage of mineralization and metal concentration, and it can be the source of metal for later remobilization by hydrothermal activities (Zhang et al., 2024).

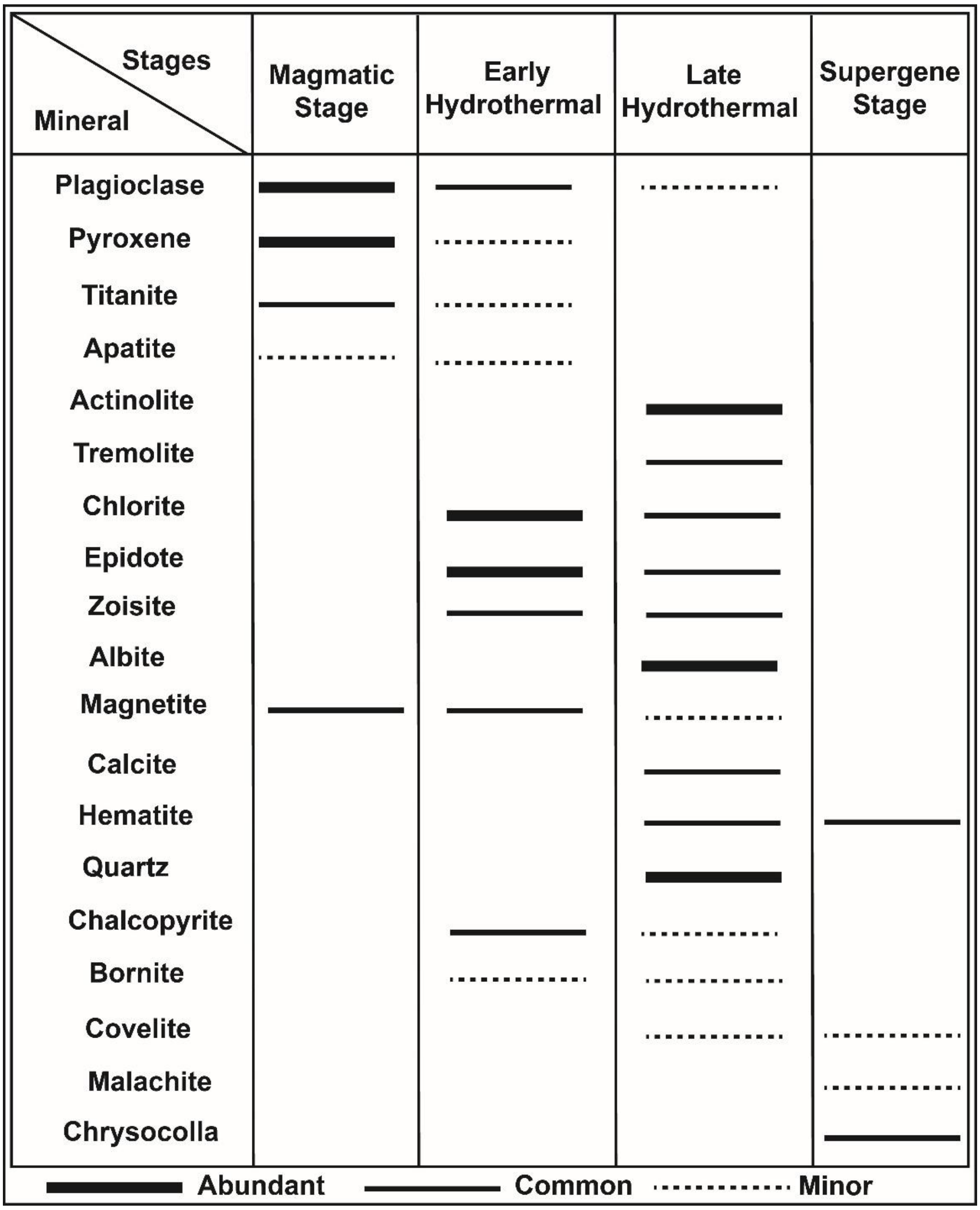

Figure 12. The paragenetic sequence of minerals across the stages of mineralization in the Galalla area.

In the early hydrothermal stage, primary silicate minerals are altered to minerals such as epidote, chlorite, and quartz by hydrothermal fluids. Simultaneously, the formation of sulfidic minerals such as chalcopyrite and accessory bornite as vein and fracture filling reflects initial metal transportation by hot, metal-rich hydrothermal fluids, which is an indicator of epithermal systems (Canet et al., 2011).

The secondary sulfides, such as bornite, covellite, and Fe-oxide (hematite), were formed in the late hydrothermal stage due to interaction of hydrothermal fluids with host rocks, which is an indicator for evolving fluid compositions during late-stage mineralization. Carbonatization, which is indicated by calcite formation, is an indicator for hydrothermal neutralization (Torró et al., 2012).

The supergene enrichment stage is associated with oxidation and weathering processes, which in turn promote the formation of secondary copper minerals such as chrysocolla and malachite. The sequence of mineralization observed is consistent with a typical hydrothermal system superimposed on a magmatic host.

SEM-EDS analysis and elemental mapping reveal that some magnetite and hematite in the Galalla samples are commonly associated with the alteration rims of chalcopyrite grains, often exhibiting zoning textures (Figure 8). The high Cu contents detected in the outer zones of these Fe-oxides are interpreted as the result of hydrothermal alteration and oxidation of chalcopyrite, rather than primary incorporation into the oxide crystal structure. This replacement process likely involved Fe mobilization and Cu retention during fluid-rock interaction, producing Fe-oxides (magnetite and hematite) enriched in Cu, either as fine inclusions or adsorbed at grain boundaries (Klevenz et al., 2011; Toner et al., 2016). These textures and other textures, such as replacement, exsolution, and colloform, indicate the multi-stage nature of mineralization, which involves hydrothermal, supergene, and remobilization processes (Gao et al., 2017).

5.3. Economic Implications and Exploration Potential

The mineralization in the Galalla area, characterized by Cu-bearing sulfides, titanite, magnetite, hematite, and phosphates, has significant economic potential, particularly within the framework of hydrothermal deposits. The area has a good potential for the mineralization of Cu, Fe, and Ti (this study), and Zn (Mustafa et al., 2023a, 2023b). The data of the present study relative to the upper continental crust (UCC) show an elevation in the concentration of metals such as Fe, Ti, and some of the REE (Table 6). The Trace elements such as Cu, Ag, Cd, and Sb show enrichment relative to UCC (Table 6).

To further evaluate the economic potential of the Galalla deposit, a systematic exploration approach is recommended. The recommended methods are detailed geochemical surveys, geophysical surveys such as induced polarization (IP) and magnetometric and gravimetric surveys, and finally drilling of the potential area. The economic potential of copper mineralization in Kurdistan is significant, given the region's geological endowment and the global demand for copper. The region has been identified as a promising area for copper exploration, with several deposits already known and others suspected to exist based on geological surveys (Al-Bassam, 2013; V. Sissakian, 2018). The development of the region's copper resources has the potential to contribute significantly to the local and national economy, while also helping to meet the global demand for this important metal.

Table 6. The concentration factor for the average concentration of different elements in the gabbro and basalt in the area (UCC is according to Rudnick & Gao, 2014).

Major elements (wt.%) and REE (ppm)				Trace Elements (ppm)			
Elements	**Gabbro**	**Basalt**	**UCC**	**Elements**	**Gabbro**	**Basalt**	**UCC**
SiO_2	0.92	0.84	66.62	Ag	3.77	6.60	0.05
Al_2O_3	0.89	1.00	15.40	As	1.06	2.29	4.80
CaO	1.64	1.95	3.59	Ba	0.07	0.09	624.00
Fe_2O_3	1.49	2.13	5.04	Cd	2.50	5.74	0.09
K_2O	0.03	0.09	2.80	Co	1.21	1.25	17.30
MgO	1.42	1.21	2.48	Cr	2.20	0.90	92.00
MnO	1.05	1.58	0.10	Cs	0.10	0.11	4.90
Na_2O	1.19	0.98	3.27	Cu	52.49	132.49	28.00
P_2O_5	0.72	0.94	0.15	Li	0.45	0.52	21.00
TiO_2	0.75	1.20	0.64	Mo	0.48	0.89	1.10
La	0.29	0.38	31.00	Nb	0.43	0.61	12.00
Ce	0.35	0.41	63.00	Ni	0.86	0.38	47.00
Pr	0.49	0.67	7.10	Pb	0.08	0.21	15.00
Sm	1.16	1.56	27.00	Rb	0.01	0.05	84.00
Eu	1.69	2.48	4.70	S	0.57	0.60	621.00
Gd	1.61	2.20	1.00	Sb	1.31	1.38	0.40
Sc	1.36	1.21	4.00	Sn	0.69	1.20	2.10
Tb	1.89	2.57	14.00	Sr	0.46	0.70	320.00
Dy	2.24	2.97	0.70	Ta	0.36	0.54	0.90
Er	2.27	3.07	3.90	Th	0.13	0.13	10.50
Tm	2.50	3.33	2.30	U	0.06	0.08	2.70
Yb	2.51	3.36	0.30	V	0.48	0.73	97.00
Lu	2.26	3.12	2.00	Zn	0.74	1.94	67.00
Y	2.17	2.83	0.31	Zr	0.15	0.17	193.00

6. Conclusions

The Galalla area, located within the Penjween-Walash subzone of the Iraqi Zagros Suture Zone, presents a complex assemblage of mafic to ultramafic rocks that host significant hydrothermal copper mineralization. Field observations, petrography, mineral chemistry, and geochemical data collectively support a multi-phase mineralization history. The studied gabbroic and basaltic rocks exhibit intense hydrothermal alteration, including chloritization, epidotization, silicification, and spilitization, which facilitate the mobilization and concentration of copper and iron-bearing minerals. The ore assemblage is dominated by chalcopyrite, chalcocite, covellite, and chrysocolla, along with magnetite and hematite, which display clear replacement textures and zonal alteration patterns indicative of fluid-rock interaction.

The geochemical signature of the mineralized rocks shows elevated concentrations of Cu (up to 7536 ppm), and some REEs (La, Ce, Nd. The discovery of Cu-bearing phosphates and tube-like apatite structures provides further evidence of phosphate-associated remobilization of metals by hydrothermal fluids. These mineralogical and geochemical features point to a magmatic-hydrothermal system, where primary magmatic phases were overprinted by metal-rich fluids and subsequently modified by supergene processes. The Galalla deposit, though still in the early stages of evaluation, holds promising economic potential for copper and associated elements, meriting further exploration through detailed geophysical and drilling campaigns.

Acknowledgments

The author expresses sincere gratitude to the Scientific Research Center of Soran University for its invaluable support in facilitating both the SEM and XRD analyses.

References

Ahmed, I., Kettanah, Y., & Ismail, S. (2020). Genesis and tectonic setting of high-Cr podiform chromitites of the Rayat ophiolite in the Zagros Suture Zone, northeastern Iraq. *Ore Geology Reviews*. https://doi.org/10.1016/j.oregeorev.2020.103583

Alavi, M. (1994). Tectonics of the Zagros orogenic belt of Iran: new data and interpretations. *Tectonophysics*, *229*(3–4), 211–238. https://doi.org/10.1016/0040-1951(94)90030-2

Alavi, M. (2004). Regional stratigraphy of the Zagros fold-thrust belt of Iran and its proforeland evolution. *American Journal of Science*, *304*(1), 1–20. https://doi.org/10.2475/ajs.304.1.1

Al-Bassam, K. (2013). Mineral resources in the Kurdistan region. *Iraqi Bulletin of Geology and Mining*, *9(3)*, 103–128.

Ali, S., Buckman, S., Aswad, K., Jones, B., Isamil, & Nutman, A. (2012). *Geochemistry, Geochronology and Petrogenesis of Late Cretaceous Hasanbag Ophiolite-Arc Rocks in the Kurdistan Region of the NE Iraqi Zagros Thrust Zone*.

Al-Jubury, H. E., Agha, M. Y. T., & Aqrawi, A. M. (2023). Petrography and Geochemical Relationships of the Ultramafic Rocks in Galalah area within Erbil Governorate, NE Iraq. *Iraqi Journal of Science*, 228–252.

Al-Qayim, B., Ghafor, I., & Jaff, R. (2014). Contribution to the stratigraphy of the Walash Group, Sulaimani area, Kurdistan, Iraq. *Arabian Journal of Geosciences*, *7*, 181–192.

Bruno, P., Ricciardi, G., Petrillo, Z., Di Fiore, V., Troiano, A., & Chiodini, G. (2007). Geophysical and hydrogeological experiments from a shallow hydrothermal system at Solfatara Volcano, Campi Flegrei, Italy: Response to caldera unrest. *Journal of Geophysical Research*, *112*, B06201. https://doi.org/10.1029/2006JB004383

Canet, C., Franco, S. I., Prol-Ledesma, R. M., Gonzáléz-Partida, E., & Villanueva-Estrada, R. E. (2011). A Model of Boiling for Fluid Inclusion Studies: Application to the Bolaños Ag–Au–Pb–Zn Epithermal Deposit, Western Mexico. *Journal of Geochemical Exploration*, *110*(2), 118–125. https://doi.org/10.1016/j.gexplo.2011.04.005

Cannell, J. (2005). Geology, Mineralization, Alteration, and Structural Evolution of the El Teniente Porphyry Cu-Mo Deposit. *Economic Geology*, *100*(5), 979–1003. https://doi.org/10.2113/100.5.979

Cao, Y., Wang, C., Yeung, N., & Zhang, Z. (2019). Iron Isotope Systematics of the Panzhihua Mafic Layered Intrusion Associated With Giant Fe-Ti Oxide Deposit in the Emeishan Large Igneous Province, SW China. *Journal of Geophysical Research: Solid Earth*, *124*. https://doi.org/10.1029/2018JB016466

Cox, D. P., Lindsey, D. A., Singer, D. A., Moring, B. C., & Diggles, M. F. (2003). Sediment-hosted copper deposits of the world: Deposit models and database. *Open-File Report*, *2003–107*.

Davidson, P., Kamenetsky, V., Cooke, D., Frikken, P., Hollings, P., Ryan, C., Achterbergh, E., Mernagh, T., Skarmeta, J., & Serrano, L. (2005). Magmatic Precursors of Hydrothermal Fluids at the Rio Blanco Cu-Mo Deposit, Chile: Links to Silicate Magmas and Metal Transport. *Economic Geology*, *100*, 963–978. https://doi.org/10.2113/gsecongeo.100.5.963

Efimenko, N., Schneider, J., Spangenberg, J., Chiaradia, M., Adatte, T., & Föllmi, K. (2014). Formation and age of sphalerite mineralization in carbonate rocks of Bajocian age in the Swiss Jura Mountains: Evidence of Mesozoic hydrothermal activity. *International Journal of Earth Sciences*, *103*. https://doi.org/10.1007/s00531-014-1015-8

Gao, H., Zhang, Y., Gu, X., & Li, J. (2017). Ore Genesis of the Xiyi Pb-Zn Deposit, Western Yunnan Province, China: Geologic, Fluid Inclusion, and Isotopic (C-H-O-S-Pb) Evidence. *Geological Journal*, *53*(3), 1165–1185. https://doi.org/10.1002/gj.2949

Gawlick, H.-J., Frisch, W., Hoxha, L., Dumitrica, P., Krystyn, L., Lein, R., Missoni, S., & Schlagintweit, F. (2008). Mirdita Zone ophiolites and associated sediments in Albania reveal Neotethys Ocean origin. *International Journal of Earth Sciences*, *97*, 865–881.

Grosche, A., Klemd, R., Denkel, K., Keith, M., Haase, K., Voudouris, P., Alfieris, D., & Wiedenbeck, M. (2023). Sources, transport, and deposition of metal(loid)s recorded by sulfide and rock geochemistry: constraints from a vertical profile through the epithermal Profitis Ilias Au prospect, Milos Island, Greece. *Mineralium Deposita*, *58*. https://doi.org/10.1007/s00126-023-01170-2

Hastie, A. R., Kerr, A. C., Pearce, J. A., & Mitchell, S. F. (2007). Classification of altered volcanic island arc rocks using immobile trace elements: development of the Th–Co discrimination diagram. *Journal of Petrology*, *48*(12), 2341–2357.

Ismail, S. (2008). The Occurrence Of The Platinum Group Minerals Laurite In The Ophiolitic–Chromitite Rocks, Zagross Thrust Zone, Rayat Area, N-E Iraq. *University of Sharjah Journal of Pure & Applied Sciences*, *5*.

Jassim, S. Z., & Guff, J. C. (2006). *Geology of Iraq*.

Klevenz, V., Bach, W., Schmidt, K., Hentscher, M., Koschinsky, A., & Petersen, S. (2011). Geochemistry of Vent Fluid Particles Formed During Initial Hydrothermal Fluid-Seawater Mixing Along the Mid-Atlantic Ridge. *Geochemistry Geophysics Geosystems*, *12*(10), n/a-n/a. https://doi.org/10.1029/2011gc003704

Latif, D., Mohammad, Y., & Baziany, M. (2022). Mineralogy and Origin of the Manganese Deposit in the Sulaimani Province, Kurdistan Region of Iraq: Insight to Serpentinization-Induced Manganese Production Scenario. *Iraqi Geological Journal*, *55*, 178–200. https://doi.org/10.46717/igj.55.1F.15Ms-2022-06-30

Lawa, Lawa, F. A., Koyi, H., & Ibrahim, A. (2013). Tectono-stratigraphic evolution of the NW segment of the Zagros fold-thrust belt, Kurdistan, NE Iraq. *Journal of Petroleum Geology*, *36*(1), 75–96. https://doi.org/10.1111/jpg.12543

McDonough, W. F., & Sun, S. (1995). The composition of the Earth. *Chemical Geology*, *120*, 223–253.

Merza, T., & Abdalla, S. (2023). Petrography and Mineralogy of the iron ore from Nawgwezany Mishao area–Shalair Valley, KRG - Iraq: Insights on the Genesis. *Iraqi Journal of Science*, *Vol. 64*, pp 5355-5373. https://doi.org/10.24996/ijs.2023.64.9.15

Mirza, T. A., & Rashid, S. G. (2018). Mineralogy, Fluid inclusions, and stable isotopes study constraints on genesis of sulfide ore mineral, Qaladiza area, Qandil Series, Iraqi Kurdistan Region. *Arabian Journal of Geosciences*, *11*, 1–15.

Mohajjel, M., & Fergusson, C. L. (2014). Jurassic to Cenozoic tectonics of the Zagros Orogen in northwestern Iran. *International Geology Review*, *56*(3), 263–287.

Mohammad, Y., & Cornell, D. (2017). U-Pb zircon geochronology of the Daraban leucogranite, Mawat ophiolite, Northeastern Iraq: A record of the subduction to collision history for the Arabia-Eurasia plates. *Island Arc*, *26*, e12188. https://doi.org/10.1111/iar.12188

Mohammad, Y., Cornell, D., Qaradaghi, J., & Mohammad, F. (2014). Geochemistry and Ar–Ar muscovite ages of the Daraban Leucogranite, Mawat Ophiolite, northeastern Iraq: Implications for Arabia–Eurasia continental collision. *Journal of Asian Earth Sciences*, *86*, 151–165. https://doi.org/10.1016/j.jseaes.2013.09.029

Mohammad, Y., Latif, D., Pirouei, M., & Omer, D. (2024). Mineralogical and geochemical features of the Sirna Mn-Fe deposit in the Kurdistan region, northeastern Iraq: Unveiling the formation of a Mn-Fe silica gel plume via serpentinization hydrothermal mechanisms. *Resource Geology*, *74*(1), e12336.

Mohammad, Y., Latif, K., & Azizi, H. (2023). Late Cretaceous-Paleocene Arc and Back-Arc System in the Neotethys Ocean, Zagros Suture Zone. *Minerals*, *13*, 1367. https://doi.org/10.3390/min13111367

Mohammad, Y., & Yara, I. (2018). *Iron-copper mineralization associated with metagabbro in Mirawa Village, Kurdistan region, northeastern Iraq*. 20–22.

Mondillo, N., Boni, M., Balassone, G., Forrester, N., Putzolu, F., & Santoro, L. (2020). Mineralogy and Genesis of the Kihabe Zn-Pb-v Prospect, Aha Hills, Northwest Botswana. *Minerals*, *10*(8), 685. https://doi.org/10.3390/min10080685

Moores, E. M., Kellogg, L. H., & Dilek, Y. (2000). Tethyan ophiolites, mantle convection, and tectonic “historical contingency”: A resolution of the “ophiolite conundrum.” *Special Paper 349: Ophiolites and Oceanic*

Crust: New Insights from Field Studies and the Ocean Drilling Program, *349*(December 2015), 3–12. https://doi.org/10.1130/0-8137-2349-3.3

Mustafa, T., Merza, T., & Kalaitzidis, S. (2023a). Genesis of Sulfide Mineralization in the Gallala Area, Kurdistan Region, Iraq: Constraints from Major and Trace Elements of Sulfide Ore Mineralization and their Host Rocks. *Iraqi Geological Journal*, *56*, 1–22. https://doi.org/10.46717/igj.56.2F.1ms-2023-12-7

Mustafa, T., Merza, T., & Kalaitzidis, S. (2023b). Petrographical and Geochemical Features of Sulfide Mineralization in the Walash Group, Gallala Area, Kurdistan Region of Iraq. *Iraqi Geological Journal*, *56*, 19–36. https://doi.org/10.46717/igj.56.2E.2ms-2023-11-7

Numan, M. N. (1997). A plate tectonic scenario for the Phanerozoic succession in Iraq. *Iraqi Geological Journal*, *30*(2), 85–119.

Othman, A., & Gloaguen, R. (2013). Automatic Extraction and Size Distribution of Landslides in Kurdistan Region, NE Iraq. *Remote Sensing*, *5*(5), 2389–2410. https://doi.org/10.3390/rs5052389

Parlak, O. (2016). The tauride ophiolites of Anatolia (Turkey): A review. *Journal of Earth Science*, *27*, 901–934.

Pettke, T., Oberli, F., & Heinrich, C. (2010). The magma and metal source of giant porphyry-type ore deposits, based on lead isotope microanalysis of individual fluid inclusions. *Earth and Planetary Science Letters - EARTH PLANET SCI LETT*, *296*, 267–277. https://doi.org/10.1016/j.epsl.2010.05.007

Pirouei, M., Kolo, K., & Kalaitzidis, S. P. (2020). Hydrothermal listvenitization and associated mineralizations in Zagros Ophiolites: Implications for mineral exploration in Iraqi Kurdistan. *Journal of Geochemical Exploration*, *208*. https://doi.org/10.1016/j.gexplo.2019.106404

Pirouei, M., Kolo, K., Kalaitzidis, S. P., & Mustafa Abdullah, S. (2021). Newly discovered gossanite-like and sulfide ore bodies associated with microbial activity in the Zagros ophiolites from the Rayat area of NE Iraq. *Ore Geology Reviews*, 104191. https://doi.org/10.1016/j.oregeorev.2021.104191

Pitcairn, I., Teagle, D., Craw, D., Olivo, G., Kerrich, R., & Brewer, T. (2006). Sources of Metals and Fluids in Orogenic Gold Deposits: Insights from the Otago and Alpine Schists, New Zealand. *Economic Geology*, *101*, 1525–1546. https://doi.org/10.2113/gsecongeo.101.8.1525

Rudnick, R., & Gao, S. (2014). *4.1 - Composition of the Continental Crust* (pp. 1–51).

Sharkov, E., Bortnikov, N., Zinger, T., & Chistyakov, A. (2005). Silicic Fe-Ti-oxide series of slow-spreading ridges: petrology, geochemistry, and genesis with reference to the Sierra Leone segment of the Mid-Atlantic Ridge axial zone at 6\deg N. *Russian Journal of Earth Sciences*, *7*, 1–30. https://doi.org/10.2205/2005ES000181

Sharkov, E. V, Бортников, Н. С., Zinger, T. F., & Chistyakov, A. V. (2005). Silicic Fe-Ti-Oxide Series of Slow-Spreading Ridges: Petrology, Geochemistry, and Genesis With Reference to the Sierra Leone Segment of the Mid-Atlantic Ridge Axial Zone at 6\deg N. *Russian Journal of Earth Sciences*, *7*(4), 1–30. https://doi.org/10.2205/2005es000181

Shen, J., Dai, J., Yang, K., Zhao, L., Zhang, W., Malaspina's, N., & Sternai's, P. (2024). Coeval formation and exhumation of metamorphic sole and ophiolite in the Saga ophiolitic mélange: Insights into subduction initiation of the Neo-Tethys. *Journal of Metamorphic Geology*, *42*(6), 843–865.

Sillitoe, R. H. (2010). Porphyry copper systems. *Economic Geology*, *105*(1), 3–41.

Simusokwe, M., Watanabe, Y., & Echigo, T. (2021). Hydrothermal alteration and Cu–Co mineralization at the peripheral zone (Target H) of the Kitumba iron–oxide copper–gold system, Mumbwa District, Zambia. *Resource Geology*, *71*. https://doi.org/10.1111/rge.12274

Sissakian, V. (2018). The Minerals Wealth in the Kurdistan Region, Iraq. *UKH Journal of Science and Engineering*, *2*, 23–36. https://doi.org/10.25079/ukhjse.v2n2y2018.pp23-36

Sissakian, k V. (2000). *Geological Map of Iraq. 1:1 000 000. State Company of Geological Survey and Mining, Baghdad.*

Todesco, M., Rinaldi, A. P., & Bonafede, M. (2010). Modeling of unrest signals in heterogeneous hydrothermal systems. *Journal of Geophysical Research: Solid Earth*, *115*. https://doi.org/10.1029/2010JB007474

Toner, B. M., Rouxel, O., Santelli, C., Bach, W., & Edwards, K. J. (2016). Iron Transformation Pathways and Redox Micro-Environments in Seafloor Sulfide-Mineral Deposits: Spatially Resolved Fe XAS and Δ57/54Fe Observations. *Frontiers in Microbiology*, *7*. https://doi.org/10.3389/fmicb.2016.00648

Torró, L., Villanova, C., Castillo, M. K., Campeny, M., Gonçalves, A. O., & Draper, J. C. M. i. (2012). Niobium and Rare Earth Minerals From the Virulundo Carbonatite, Namibe, Angola. *Mineralogical Magazine*, *76*(2), 393–409. https://doi.org/10.1180/minmag.2012.076.2.08

Troll, V., Weis, F., Jonsson, E., Andersson, U., Majidi, A., Högdahl, K., Harris, C., Millet, M.-A., Chinnasamy, S., Kooijman, E., & Persson Nilsson, K. (2019). Global Fe–O isotope correlation reveals magmatic origin of Kiruna-type apatite-iron-oxide ores. *Nature Communications*, *10*. https://doi.org/10.1038/s41467-019-09244-4

Vasieliev M.M. Pentelikov, V. G. (1962). *Report on prospecting exploration of Bard-i-Zard chromite occurrence and adjacent areas. Technoexport Report, No. 298, Geological Survey Mineral Investigation*.

Yassin, A., Alabidi, A., Hussain, M., Al-Ansari, N., & Knutsson, S. (2015). Copper ores in mawat ophiolite complex (Part of ZSZ), NE Iraq. *Natural Resources*, *6*(10), 514–526.

Zhang, Y. L., Zhu, J.-J., Pan, L.-C., Huang, M., Wang, D.-Z., & Zou, Z. (2024). Apatite as a Record of Magmatic–Hydrothermal Evolution and Metallogenic Processes: The Case of the Hongshan Porphyry–Skarn Cu–Mo Deposit, SW China. *Minerals*, *14*(4), 373. https://doi.org/10.3390/min14040373

About the author

Mohammad Pirouei is a geologist who specializes in economic geology and mineral exploration. His research focuses on different types of ore minerals. He is affiliated with the Petroleum Geoscience Department, Faculty of Science, Soran University, where his work centers on mineralization.

e-mail: Mohammad.askandar@soran.edu.iq